

PCCP

Accepted Manuscript



This is an *Accepted Manuscript*, which has been through the Royal Society of Chemistry peer review process and has been accepted for publication.

Accepted Manuscripts are published online shortly after acceptance, before technical editing, formatting and proof reading. Using this free service, authors can make their results available to the community, in citable form, before we publish the edited article. We will replace this *Accepted Manuscript* with the edited and formatted *Advance Article* as soon as it is available.

You can find more information about *Accepted Manuscripts* in the [Information for Authors](#).

Please note that technical editing may introduce minor changes to the text and/or graphics, which may alter content. The journal's standard [Terms & Conditions](#) and the [Ethical guidelines](#) still apply. In no event shall the Royal Society of Chemistry be held responsible for any errors or omissions in this *Accepted Manuscript* or any consequences arising from the use of any information it contains.

Versatility of electrospinning on the fabrication of fibrous mat and mesh nanostructures of bismuth ferrite (BiFeO₃) and their magnetic, photocatalytic activities

Cite this: DOI: 10.1039/x0xx00000x

Received 00th January 2012,
Accepted 00th January 2012

DOI: 10.1039/x0xx00000x

www.rsc.org/

S. Bharathkumar, M. Sakar, Rohith Vinod K., and S. Balakumar*

This study demonstrates the fabrication of electrospun bismuth ferrite (BiFeO₃/BFO) fiber mat and fibrous mesh nanostructures consisting of aligned and random fibers respectively. The formation of these one dimensional (1D) nanostructures was mediated by the drum and plate collectors in electrospinning process that yielded aligned and random nanofibers of BFO respectively. The single phase and rhombohedral crystal structure of the fabricated 1D BFO nanostructures are confirmed through X-Ray Diffraction (XRD) studies. X-ray Photoelectron Spectroscopy (XPS) studies indicated that the fabricated fibers are stoichiometric BFO with native oxidation states +3. The surface texture and morphology are analyzed using the Field Emission Scanning Electron Microscopy (FESEM) and High Resolution Transmission Electron Microscopy (HRTEM) techniques. The average size of fibers in mat and mesh nanostructures is found to be 200 nm and 150 nm respectively. The band gap energy of BFO mat and mesh deduced from their UV Diffuse Reflectance Spectra (UV-DRS) that found to be 2.44 eV and 2.39 eV respectively which evidenced the improved visible light receptivity of BFO mesh compared to that of the mat. Magnetization studies by Super Conducting Quantum Interference Device (SQUID) magnetometer revealed the weak ferromagnetic properties of BFO mesh and mat that could be emerged due to the dimension induced suppression of cycloidal spin structures. The photocatalytic degradation property of the fibrous mesh is found to be enhanced than that of the mat. This could be attributed to the reduced band gap energy and improved semiconductor band-bending phenomenon in the mesh that favoured the transportation of excited charge carriers to the photocatalyst-dye interfaces and the production of more number of reactive species that lead to the effective degradation of the dye molecules.

1. Introduction

The reputation of multiferroic materials is owing to the co-existence of different types of ferroic orders such as ferroelectric, (anti-)ferromagnetic, ferroelastic, etc., in their *single phase states*.¹ Among the existing multiferroic materials, bismuth ferrite (BiFeO₃/BFO) is a well-established natural multiferroic material that shows ferroelectric and anti-ferromagnetic properties at room temperature.² BFO is considered to be an exemplary material for the investigation of the origin of multiferroic properties in materials.³ Eventually, such exploration and the insights derived thereof led to the production of artificial multiferroic materials.^{3,4} Besides, multiferroic properties, BFO is also explored for their photocatalytic properties towards the degradation of organic pollutants and water splitting applications.⁵ The narrow band

gap energy (~2.3 eV) of BFO makes it a very promising candidate to be driven by visible light for such photo-driven applications.^{5,6} Intense research on BFO that focused on its photocatalytic applications are being propelled as its multiferroic properties also aid in achieving the necessary conditions for the enhanced photocatalytic process in BFO. Accordingly, it is possible to control and manipulate the transportation of charge carriers through the ferroelectric properties,⁷ and improving its magnetic properties also favours the separation of BFO from the dye medium.⁸

In pursuit of enhancing the photocatalytic properties, BFO has been modified in its chemical composition such as substitution, composites, metal decoration,^{8,9} and physical structures like anisotropic nanostructures with different morphologies, and sizes.¹⁰ Among the various anisotropic nanostructures, one dimensional (1D) structures, especially, the

fiber nanostructures are gaining significant attention due to their enhanced physical as well as chemical properties that are governed by their confined structures and subsequent modification in the electronic properties of the materials.¹¹ For instance, considering the photocatalytic process, enhancing the carrier diffusion length and recombination resistance are the two major essential criteria for improving the photocatalytic activity of a photocatalyst.¹² Such manipulations can be effectively achieved in the 1D nanostructured photocatalyst.¹³

Electrospinning is an effective and straightforward technique to fabricate 1D fiber based nanostructures with controlled dimensions and morphologies. The electrospinning process can be divided into three stages, (i) Preparation of electrospinning solution (choice of solvents, polymers, optimization of the solution concentration, viscosity of the solution, etc.), (ii) Controlling the electrospinning parameters (applied voltage, flow rate, collector type, etc.), and (iii) Optimization of the annealing conditions (annealing temperature, ramping rate, annealing time, etc.). A meticulous control over the parameters in each stage would enable effective manipulations of the morphology of fibers.¹⁴ For instance; fibers with different morphologies can be produced by changing the polymer concentration, solvents and fiber collectors. An effective control over the applied voltage and collector type would lead to the formation of fibers with different sizes and distributions. Also, the annealing conditions would lead to the breaking of fibers into smaller lengths.¹⁵⁻¹⁷ Despite the fact that electrospinning offers a facile way of fiber fabrications, the optimization process for obtaining fibers with desired features is quite complex as it consists of a broad range of conditions to be controlled. However, it is possible that the arrangement of fibers can be tuned by using different types of fiber collectors such as drums, plates and discs. The fabrication of fibers with such configurations also exhibits property variations as they establish different levels of interactions with the surrounding phases such as solid, liquid, and gas, as well as enhanced responses to the external stimuli such as magnetic or electrical field, thermal energy, etc.¹⁸

In this perspective, we report herein the fabrication of BFO mat and fibrous mesh nanostructures by electrospinning technique, which is exclusively mediated by different types of collectors. In morphological perspective, the mats are long-range uniformly aligned fibers, while the meshes are completely random in their distribution and alignments. Fig. 1(a)-(b) shows well known objects such as 'household mats' and 'noodles' which could be analogical to these fibrous mats and mesh nanostructures respectively reported in this present study. The fabricated BFO 1D nanostructures were characterized for their magnetic properties and photocatalytic abilities towards the degradation of organic dye under exposure of natural sunlight. The fabrication of mat like fibrous structures of BFO and TiO₂ based materials has been reported in the literatures and studied for their photocatalytic properties.¹⁹ However, our approach of experimental design to obtain the mat and mesh nanostructures are relatively facile and

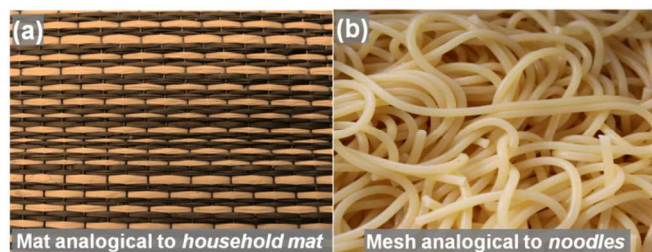


Fig. 1 Common objects (a) household mat and (b) noodles that are analogical to the fabricated 1D fibrous mat and mesh nanostructures reported in this study.

showed enhanced properties that ascribed to the controlled size, morphological parameters of the fabricated nanostructures.

2. Experiment

2.1. Fabrication of BFO fiber mat and mesh

In a typical procedure, 0.8 M of bismuth nitrate [Bi(NO₃)₃·6H₂O] and iron nitrate [Fe(NO₃)₃·9H₂O] were taken and dissolved in 5 ml of glacial acetic acid. An amount of 1 g of polyvinyl pyrrolidone, (PVP, M.W. 13, 00, 000) was then dissolved in 5 ml double distilled water and added to the above solution. Thereafter, these solutions were mixed up and stirred homogeneously for 6 h. This homogeneous solution was taken in a plastic syringe equipped with stainless needle and loaded into the electrospinning system. An optimized high electrical voltage of 15 kV was applied to the needle at a flow rate of 0.2 ml/h, and the fibers were collected in drum and plate collectors. The as-spun BFO/PVP fibers were further annealed at 550 °C for 2 h, for the BiFeO₃ phase formation. The annealing temperature was deduced from the thermogravimetric weight loss curves of the as-spun samples as discussed in Section 3.1.

A schematic representation of the electrospinning process with different fiber collectors along with the photographic images of as-spun and annealed BFO mat and mesh nanostructures are shown in Fig. 2(a)-(f) respectively. Figure 2(e) shows the as-spun fibers peeled out from the drum collector.

2.2. Photocatalytic experiment

In a typical photocatalytic experiment, an amount of 10 mg of methylene blue (MB) blue dye was dissolved in 1000 ml of double distilled water to prepare the stock solution. 5 mg of BFO photocatalyst was then added to 100 ml of dye solution taken from the stock. Further, this photocatalyst-dye solution mixture was kept in the dark and stirred for 20 min to attain absorption-desorption equilibrium. The subsequent degradation of dye in terms of optical absorbance characteristics was recorded at a periodical interval using UV-Visible absorption spectrometer. The experiments were carried out in a tropical climate (Geographical location- Chennai; 13.04° N and 80.17° E on the Southern-East coast of India, Time between 10:00 am and 3:00 p.m., outside temperature: 29°C to 31°C) and the intensity of sunlight was measured every 30 min by using LT-

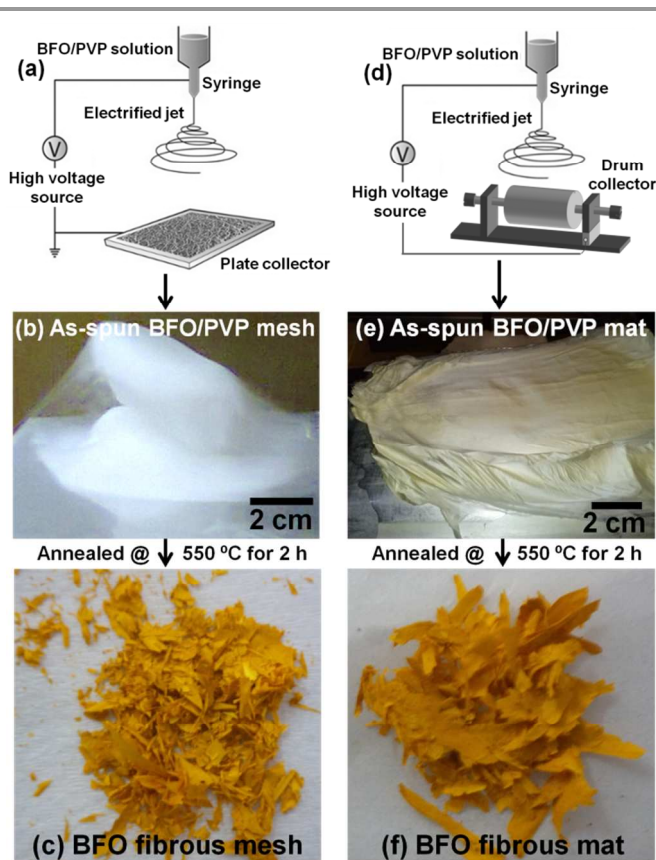


Fig. 2 Schematic representation of the electrospinning process and the photographic images of BFO (a) Fibrous mesh in plate collector, (b) As-spun mesh (c) Annealed mesh, (d) Fiber mat in drum collector, (e) As-spun mat, (f) Annealed mat.

Lutron LX-10/A digital Lux meter (TES Electrical Electronic Corp. Taiwan), wherein the average intensity of sunlight was monitored to be $1.2 \times 10^5 \pm 100$ lux.

2. 3. Materials characterizations

The fabricated materials were characterized for their thermal analysis by thermo-gravimetric analyzer (TGA-NETZSCH STA 449 F1 Jupiter), structural analysis by X-ray diffraction technique (XRD-PANalytical Instruments), chemical state analysis by X-ray photoelectron spectroscopy (XPS-Omicron Nanotechnologies), morphological analysis by field emission scanning electron microscope (FESEM-Hitachi HighTech SU6600), high resolution transmission electron microscope (HRTEM-Techni G2 S-TWIN, FEI), magnetic characteristics by super conducting quantum interference device magnetometer (SQUID-Quantum Design) and optical characteristics by UV-Visible absorption/diffuse reflectance spectroscope (UV-Vis Abs/DRS-Perkin Elmer). The photoluminescence studies were carried out by using photoluminescence spectrophotometer (PL-HORIBA Jobin Yvon's LabRAM systems) to probe the generation of OH radicals by the samples.

2. 4. Estimation of hydroxyl radicals

The efficiency of hydroxyl radical production by the BFO 1D nanostructures was estimated using PL technique,²⁰ where the terephthalic acid (TA) was used as a probe molecule. This mechanism involves the conversion of TA into a fluorescent molecule, 2-hydroxyterephthalic acid (HTA) via their reaction with OH radicals that produced by the photocatalyst²⁰ as shown in Fig. 3.

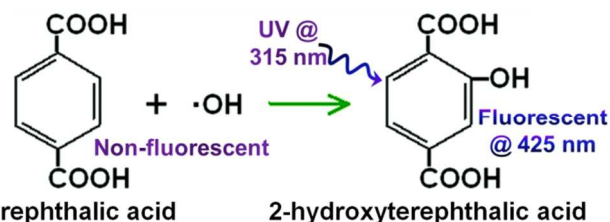


Fig. 3 Formation of fluorescent 2-hydroxyterephthalic acid via the reaction of OH radicals with terephthalic acid.

In the typical procedure, 0.1 mmol TA was dissolved in 100 ml NaOH aqueous solution to make 100 ml of 0.025 mmol TA solution, and then 0.25 g of photocatalyst was added to that 100 ml TA solution. The solution was sonicated for several minutes under dark condition and then exposed under the sunlight. The reacted solution was centrifuged to separate the catalyst and performed the PL measurements using fluorescence spectrophotometer with the excitation wavelength of 315 nm.

3. Results and discussions

3. 1. Thermo-gravimetric Analysis (TGA)

The thermo-gravimetric (TG) weight loss of the as-spun BFO/PVP aligned fiber mat and fibrous mesh were recorded in the temperature range from 30 °C to 1000 °C and the graphs are displayed in Fig. 4.

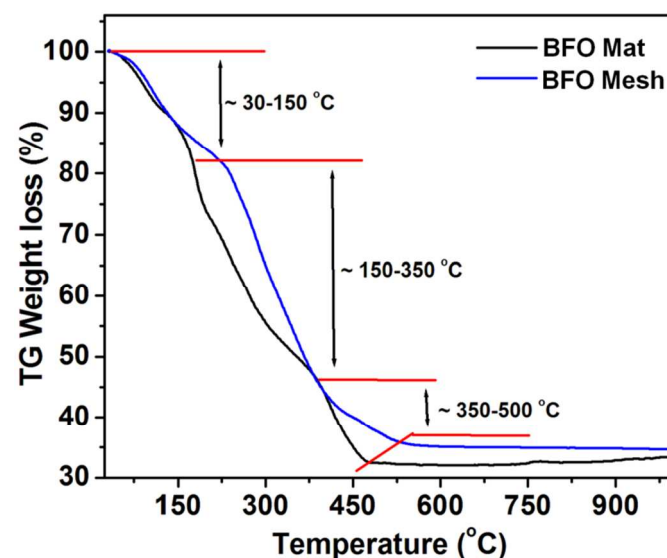


Fig. 4 Thermo-gravimetric weight loss curves of as-spun BFO mat and mesh.

The TG curves showed three stages of weight loss in the temperature range 30 °C – 150 °C, 150 °C – 350 °C and 350 °C – 500 °C. However, there is a noticeable difference in the curves that may be associated with the distribution of PVP in the as-spun samples. It is possible that the distribution of PVP molecules would be large and uneven in the as-spun mesh compared to the fibers because of their deposition mode on the collector. This can be corroborated with the obtained photographic images of the as-spun samples as shown in Fig. 2(b) & (e), where the collection of fibers in the plate collector leads to a direct deposition of fibers and establishes a random interaction between the overlapped layers. On the other hand, the drum collector collects the fibers that are akin to the weaving process, where it may induce internal strains in the fibers and also lead to an ordered alignment of the fibers. Therefore, the difference in the obtained TG curves would be due to the uneven decomposition of PVP molecules from the as-spun samples.

The first decomposition stage between 30 °C – 150 °C is due to the release of adsorbed water from the BFO/PVP fibers.²¹ The second decomposition in the temperature range 150 °C – 350 °C, is the decomposition temperature range of PVP, where the breaking of the side groups of PVP (pyrrolidone) takes place.²¹ The third decomposition stage in the temperatures between 350 °C – 500 °C could be due to the combustion and removal of the carbonized residues of PVP along with further decomposition of BFO.²² Finally, the plateau region observed in the temperature range from 500 °C – 1000 °C indicates that there are no residues to be decomposed further. Therefore, the annealing parameters such as the annealing temperature and time were optimized to be 550 °C and 2 h respectively for both the samples towards the required phase formation.

3. 2. Phase and crystal structure analysis

The crystal phase and structure identification of the annealed BFO mat and mesh nanostructures were carried out using XRD technique and the obtained patterns are shown in Fig. 5(a)-(b).

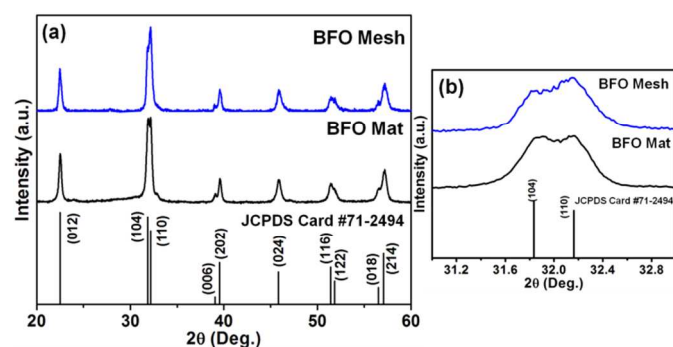


Fig. 5 XRD pattern of (a) BFO mat and mesh, (b) shift and merge in the doublet peaks.

The XRD patterns and indexed peaks are well matched to the JCPDS card #71-2494, from which the phase and crystal

structure of these 1D nanostructures were found to be perovskite BiFeO₃ and distorted rhombohedral structure with *R3c* space group respectively.²³ The crystallite size of the fabricated BFO mat and mesh was calculated by using Scherrer's formula ($t = 0.9 \lambda / \beta \cos \theta$) and found to be 23 and 27 nm respectively. Further, the structural information such as lattice parameters ($a=b, c$) and cell volume (V) were calculated from the obtained XRD patterns using software (X'pert High Score) supplied with the X-ray diffractometer and the values are given in Table 1.

Table 1. Calculated structural parameters ($a=b, c$), cell volume (V), micro strain (ϵ) and crystallite size (t) of BFO mat and mesh nanostructures.

Material	Lattice parameters		Cell volume (V)	Micro strain (ϵ)	Crystallite size (t) nm
	$a=b$	c			
BFO Mat	5.581	13.812	430.21	0.3658	23
BFO Mesh	5.584	13.679	426.53	0.3039	27

The peak merge and shift observed in doublet peak [(104), (110)] as compared to the JCPDS peaks, as shown in Fig. 4(b) indicate the reduced structural distortion in the rhombohedral structure of perovskite BFO. These doublet peaks may further coalesce into a single peak (200) that result in the cubic phase.²⁴ In addition to this, the decrement observed in the lattice parameter value (c) for BFO mesh compared to that of the mat may also be attributed to the reduced structural distortions, where such observations were reported in the particle size dependent studies on BFO.²⁴

3. 3. Chemical state analysis

The chemical oxidation state of the elements in BFO mat and mesh was investigated using XPS technique and the corresponding spectra are shown in Fig. 6(a)-(d).

From the doublet peak of Bi 4f (Fig. 6(b)) that appeared at the BE 158.7 eV, 163.8 eV for mat and 158.3 eV, 163.5 eV for mesh corresponding to Bi 4f_{7/2} and Bi 4f_{5/2} confirmed that the Bi ions possess the native oxidation state of +3. In addition, the calculated spin-orbit splitting energy (ΔE) of these doublet Bi 4f lines is around 5.2 eV, which is also consistent with the reported theoretical value of 5.4 eV.²⁵ In BFO, the oxidation state of Fe ions are volatile compared to other elements and it often possesses multiple oxidation states that primarily indicates the existence of defects such as oxygen vacancies in BFO.²⁶ In a stoichiometric BFO, the stable oxidation state of Fe is +3, which is examined in the obtained Fe spectra of BFO mat and mesh shown in Fig. 6(c). The main peaks that appeared at the BE 711.2 eV, 725.1 eV for mat and at 710.8 eV, and 724.5 eV for mesh corresponding to Fe 2p_{3/2} and Fe 2p_{1/2} evidenced the stable +3 oxidation state of Fe ions. Further, the spin-orbit splitting energy of Fe 2p_{3/2} and Fe 2p_{1/2} is calculated to be ~ 13.6 eV which further confirms +3 oxidation state of Fe ions.²⁶ Similarly, the O 1s spectra of BFO mat and mesh obtained are found to be asymmetric and are presented in Fig. 6(d). In BFO, any imbalances that occur in its stoichiometric ratio causes the

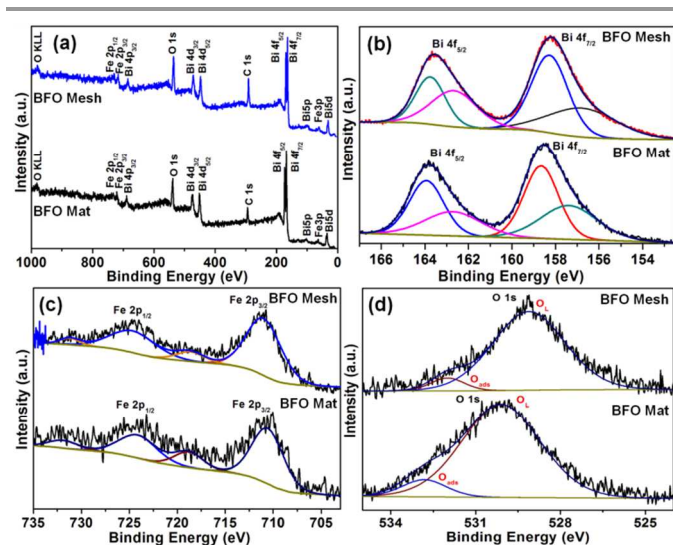


Fig. 6 XPS spectra of BFO mat and mesh, (a) Survey spectra, (b) Bi 4f, (c) Fe 2p and (d) O 1s.

changes in the oxidation state of the elements. This eventually induces defects in the BFO and they are often found to be oxygen vacancies.²⁷

Accordingly, the fitted oxygen spectra, as shown in Fig. 6(d), reveals the peaks corresponding to lattice oxygen (O_L) and chemisorbed oxygen/other species (O_C) on the surface of these nanostructures. The peaks appeared at BE 530.1 eV, 531.9 eV for mat and 530.4 eV, 532.3 eV for mesh reveal the existence of lattice (O_L) and chemisorbed oxygen species (O_C) respectively. It should be noted that the peak corresponding to oxygen vacancy (O_V) that appears at the BE around 531.2 eV, is not observed in the spectra, which indicates the stoichiometric ratio of oxygen in these nanostructures.²⁸ As the XPS analysis fundamentally helps in investigating the chemical state and associated defect structures in the materials, the results that are obtained suggest that these BFO mat and mesh nanostructures are stoichiometric with appropriate stable oxidation state and thereof the properties observed could be attributed to their intrinsic characteristics of these nanostructures and not due to the defect structures.

3. 4. Morphology analysis

The FESEM images of BFO mat and mesh nanostructures are shown in Fig. 7(a)-(d). The micrographs indicate that the major difference between the mat and mesh was their alignments, where the former is found to be orderly aligned and the later is randomly oriented. This can also be corroborated with the as-spun mesh and fibers of BFO as shown in Fig. 2(b) and (e).

It is apparently evident that the drum and plate collectors facilitate the formation of aligned fiber mat and fibrous mesh like nanostructures of BFO respectively. Further, it should also be noted that the formation of BFO phase and fiber morphology is driven by the annealing process as well. The PVP in these as-spun samples acts as a sacrificial template for the formation and growth of the 1D structures. Further, the surface texture and

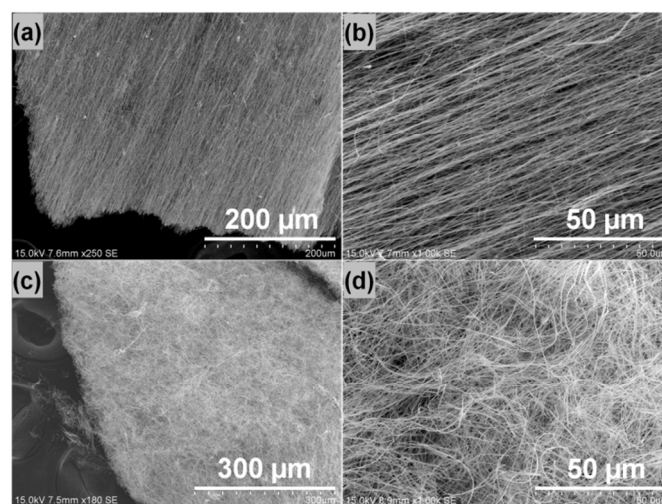


Fig. 7 FESEM micrographs of BFO (a)-(b) Mat and (c)-(d) Mesh nanostructures.

size of these 1D nanostructures imaged using HRTEM are shown in Fig. 8(a)-(d). The diameter of the fibers in the mat and mesh structure is found to be 150 nm – 300 nm and 100 nm – 200 nm respectively. The surface texture of the mat and mesh is dependent on the removal process of PVP molecules from the fibers during the annealing process and it is found to be smooth for the mat and uneven in the case of mesh.²⁹

The selected area electron diffraction (SAED) patterns of the mat and mesh are shown in the inset images of Fig. 8(a) & (c). SAED patterns appeared to be diffused rings with superimposed spots revealing the crystallite nature of the samples, the increased spots further indicating the random and complex distribution of crystallites in the mesh.³⁰

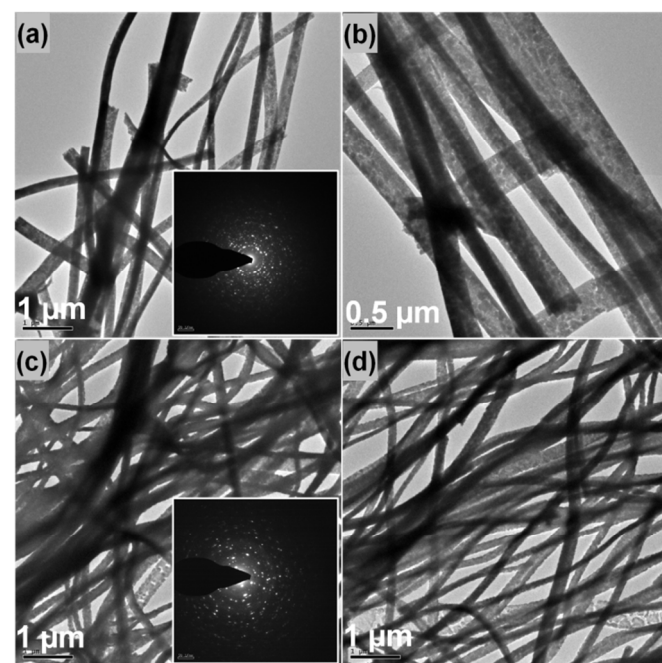


Fig. 8 HRTEM micrographs of (a)-(b) Mat and (c)-(d) Mesh. Insert image in (a) & (c) shows the SAED pattern of the respective material.

3. 5. Estimation of band gap energy

The band gap energy of the fabricated BFO mat and mesh nanostructures was estimated from their DRS graphs by applying Kubelka-Munk (KM) function³¹ as shown in Fig. 9 and its inset image respectively.

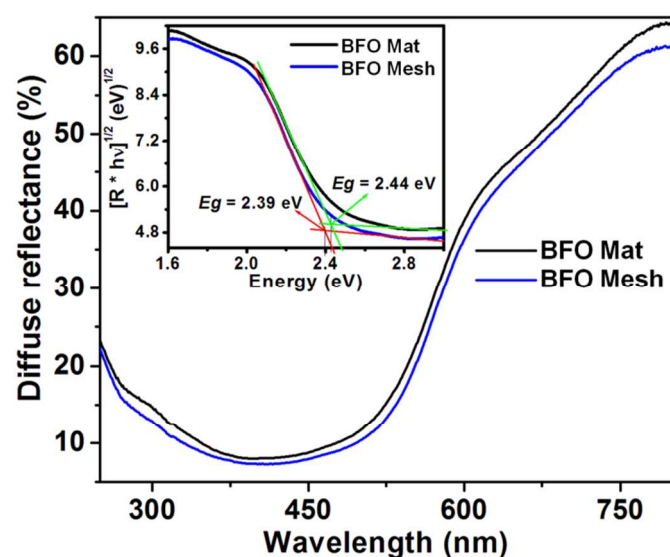


Fig. 9 Diffuse reflectance spectrum of BFO mat and mesh; Insert image shows the Kubelka-Munk (KM) plot to deduce their band gap energy.

From the KM plot, the band gap energy for BFO mat and mesh was estimated to be 2.44 eV and 2.39 eV respectively. The general strategies adopted to control the band gap energy of materials are to modify them chemically or reduce their particle size. In BFO, the formation of band gap energy is due to the overlapping of Fe 3d and O 2p states.³² Hence, any influence over the compositional (e.g. oxygen vacancy, substitution, etc.) or the structural characteristics may affect the electronic structure of BFO and thereby it leads to the alteration in the band gap energy.³³ On the other hand, controlling size/morphology of BFO would also influence the band gap energy.³⁴ Therefore, the band gap decrement observed in the mesh could be attributed to its increased crystallite size compared to that of the mat.

In addition, it is also possible that the influence over the electronic structure of BFO would be affected due to the structural changes owing to the 1D nanostructures as suggested from their XRD patterns. Such structural distortions essentially alter the bond angle in the system. In this perspective, the band gap increment found in the case of mat could be attributed to the lattice distortion owing to the alteration in the rotation of FeO₆ octahedra in the unit cells.³⁵ Such modifications might also influence the band edge positions that lead to an increase or decrease in the band gap energy of nanostructures.

3. 6. Magnetic property analysis

The room temperature field dependent magnetic properties (*M-H* hysteresis) of the fabricated BFO mat and mesh were studied by SQUID and the results are shown in Fig. 10.

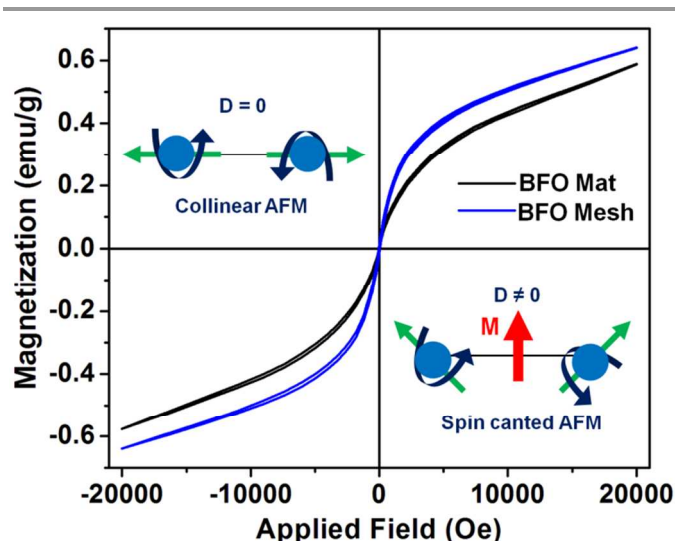


Fig. 10 Room temperature field dependent (*M-H*) hysteresis curve of BFO mat and mesh; Insert images show the manifestation of net magnetic moments due to the emergence of canted spins in BFO.

The *M-H* curve indicates the weak ferromagnetic nature of the samples. However, the magnetic property of BFO mesh is found to be slightly improved compared to the mat. It is known that the bulk BFO is an anti-ferromagnet (AFM) and it shows weak-ferromagnetism (FM) when the size is reduced to nanoscale. The manifestation of this weak FM at nanoscale BFO is essentially originating by canted spins that emerge due to the suppression of cycloidal spin structures in BFO.³⁶ The canted spins induced magnetic moments in BFO could be explained through the Dzyaloshinskii-Moriya (DM) interactions.³⁷ According to DM interactions, canted spin structures are caused by the combined actions of antisymmetric coupling and exchange interactions as shown in the inset of Fig. 10. Therefore, the origin of the weak-FM observed in the BFO mat and mesh could be their canted spin structures, which emerge due to the suppression of cycloidal spin structures facilitated by their 1D nanostructuring. This is possible as these structures are made up of inter-connected crystallites with enhanced *easy axis* of magnetization that leads to a long-range order of canted spins on the surface and become more influential to the applied magnetic field.

Further to this phenomenon, the DM interactions in spin canted materials also favour the ferroelectric polarizations in multiferroic and magneto-electric materials.³⁸ As the net magnetic moments emerge due to the canted spins, the canting angle of electronic spins influences the ferroelectric polarizations in the materials. The relationship between the magnetization (*M*), spontaneous electric polarization (*P*) and canting angle (ϕ) is given in the equations (1)-(3)³⁹.

$$M = 4\pi\alpha P \quad (1)$$

$$M = \mu_{\beta} gNS \sin \phi \quad (2)$$

$$P = (\mu_{\beta} gNS / 4\pi\alpha) \sin \phi \quad (3)$$

Where, α is magneto-electric susceptibility, μ_{β} is magnetic dipole moment of the element, $g \sim 2$ is the gyromagnetic ratio, N is the number of spins per unit volume

and S is the magnetic spin. It is evident from equation (3) that the polarization is directly proportional to the canting angle, where the existence and/or the alternation in canting angle (ϕ) induces the ferroelectric polarization in the materials. Therefore, the magnetic enhancement observed in the mesh may be associated with its ferroelectric properties, as BFO exhibits room temperature magnetic-ferroelectric properties. This phenomenon is known as ferroelectrically induced ferromagnetism.³⁹ It should be noted that the ferroelectric properties of BFO significantly favour the photocatalytic process and the improved magnetic property was also found to be favouring their separation from the dye medium towards their reusability, which is described in Section 3.7.

3.7. Photocatalytic activities

Towards an application perspective, the fabricated BFO mat and mesh were investigated for their photocatalytic ability to degrade the organic dye methylene blue (MB) under the direct irradiation of sunlight. Figure 11(a)-(c) shows the photocatalytic degradation spectra of MB dye by the mat and mesh and their photocatalytic reusability efficiency (C/C_0) ratio curves respectively.

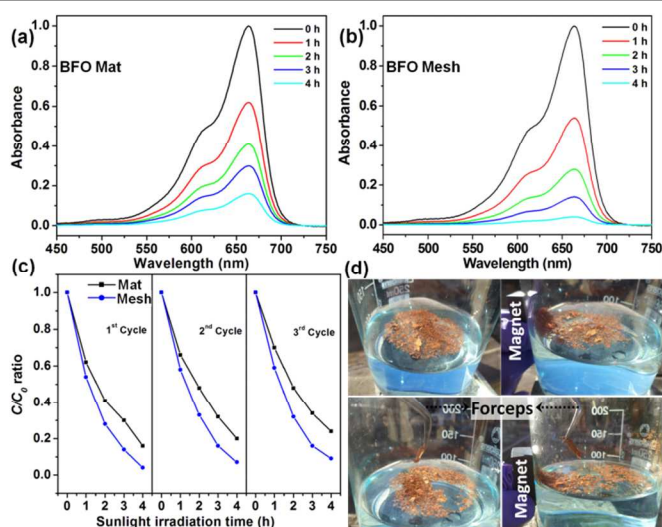


Fig. 11 Photocatalytic degradation spectra of methylene blue (MB) dye by BFO (a) Mat (b) Mesh, (c) their C/C_0 ratio graphs and (d) photographic images show the dispersion of BFO mat in MB solution and their separation by using magnet as well as manually using forceps.

It is evident from the C/C_0 graphs that at the end of 4 h of sunlight irradiation, the BFO mat and mesh degraded around 83% and 96% of dye respectively. The recovering process of the mat and mesh from the dye medium was found to be relatively easier due to their magnetically attractive property and as they were sheets/strips in nature, they could also be taken out using forceps as demonstrated in Fig. 11(d). The photocatalytic reusability efficiency of the samples was found to be consistent during repeatability tests, which indicated the stability of the BFO mat and mesh towards their reusability in their photocatalytic applications.

3.7.1. PHOTOCATALYTIC MECHANISM: Figure 12(a)-(b) shows the PL spectra of the TA solution after reacted with the BFO mat and mesh nanostructures respectively for 4 h under the direct sunlight irradiation. The curve corresponding to the 'blank' indicates no emission from the TA solution. The subsequent curves show a peak at 425 nm that reveals the presence of HTA, which converted from TA upon its reaction with OH produced by the BFO photocatalyst. The observed enhancement in the intensity of the peaks could be ascribed to the enhanced production of OH radicals with increasing time. It should be noted that the PL intensity of BFO mesh-TA solution is found to be enhanced compared to mat-TA. This shows that the meshes have higher efficiencies for OH radical production than that of the mats.

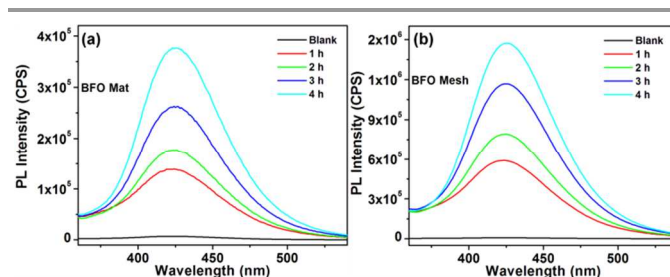


Fig. 12 PL spectra of HTA solution that reacted with BFO (a) mat and (b) mesh nanostructures under the sunlight irradiation.

When the photons fall on the photocatalyst, the electrons in valence band (VB) are excited to the conduction band (CB), inducing the production of electron-hole (e^-/h^+) pairs. These photo-induced e^-/h^+ further perform subsequent redox reactions to generate reactive species. However, the redox reactions are greatly associated to the CB and VB edge potentials of photocatalyst. The CB and VB potential of these fabricated 1D BFO nanostructures can be deduced from the Eq. (1)-(2).⁴⁰

$$E_{VB} = X - E^e + 0.5 E_g \quad (1)$$

$$E_{CB} = E_{VB} - E_g \quad (2)$$

where, X is the absolute electronegativity of the semiconductor, E^e is the energy of free electrons on the hydrogen scale (~ 4.5 eV), and E_g is the band-gap energy of the semiconductor. The value of X for BiFeO_3 is obtained, by the arithmetic mean of the electron affinity and the first ionization of the constituent atoms reported in the literatures,⁴¹ to be 5.93 eV. Thus, the CB and VB potentials of BFO mat are calculated to be 0.31 eV and 2.75 eV and for the mesh 0.33 eV and 2.72 eV respectively as shown in Fig. 13. It can be seen that the VB potential of these BFO nanostructures is more positive than the redox potential of OH^-/OH (+1.9 V/NHE), signifying that the photogenerated holes have strong oxidative capability and they can oxidize OH^- into $\cdot\text{OH}$. However, the CB potential is not negative enough to reduce O_2 to $\text{O}_2^{\cdot-}$ (-0.33 V/NHE) via electrons (Fig. 13).⁴² Thus, it is reasonable that $\cdot\text{OH}$ radicals that

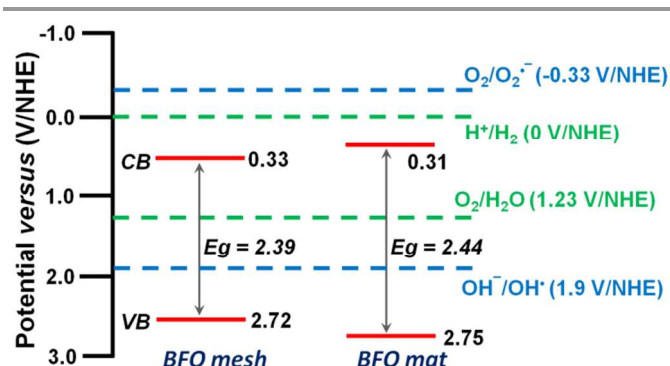
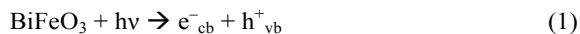


Fig. 13 Calculated valence and conduction edge potential of BFO mesh and mat nanostructures.

produced as result of the reaction between the photo-induced h^+ with OH^- are the core reactive species responsible for the degradation of the dye. The degradation path way of the dye molecules could be given as the following Eqs. (1)-(4).



Therefore, the effective separation of charge carriers and rich availability of holes are the major cause of the observed enhanced photocatalytic activity of the $BiFeO_3$ nanostructures.

The relative photocatalytic enhancement of BFO mesh could also be attributed to its intrinsic properties and the enhanced interaction with the surrounding dye molecules. It is evident from the micrographs that the BFO mesh is found to be complex in nature that might have led the dye molecules to be strongly adsorbed on its surface. Consequently, it was found during the photocatalytic experiment that the mesh was largely dispersed in the dye medium compared to the mat. These observations essentially showed the enhanced interaction of mesh with the surrounding liquid medium and hence with the dye molecules. Such a possibility leads to the BFO mesh having more number of reactive sites compared to the mat. In addition, as BFO mesh, with loosely packed structure, has improved surface interaction with dye molecules, the photo-generated carriers are effectively separated and participated in the surface redox reactions. This could suppress the recombination of e^-/h^+ and increase the production of $\bullet OH$ radicals through the generated holes. Hence, better surface adsorption and improved catalytic activity of mesh led to the enhanced degradation efficiency as compared to the mat morphology.

Apart from such physical interactions between the photocatalyst and dye molecules, the intrinsic properties of the

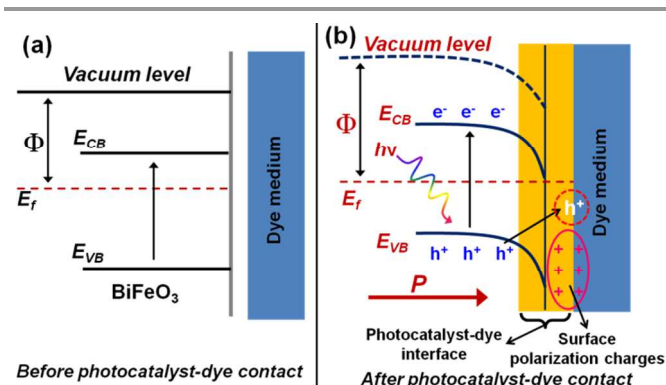


Fig. 14 Schematic representation of the band bending process in BFO nanostructures during (a) before and (b) after contact with the dye medium that depicts the bending phenomenon and surface polarization mediated transportation of excited charge carriers in these 1D BFO nanostructures.

mesh, such as smaller band gap energy and possible reduced distortions in the crystal structure also play a significant role in the photocatalytic enhancements.⁴³ It is inferred from the XRD and magnetization results that the reduced structural distortion as manifested in BFO mesh as well as its enhanced magnetic properties, which is ascribed as the ferroelectrically induced ferromagnetism, might have influenced its electrical polarization property that essentially resulted in reduced recombination possibilities in BFO mesh compared to mat.⁴⁴

The process of band bending phenomenon induced charge carrier manipulations in BFO is a tremendous possibility in the photocatalytic process. It offers control over the carrier transportation in photocatalytic process via the band bending phenomenon where the band edge positions (valence band and conduction band) of the photocatalyst would be bent at the photocatalyst-dye interface region⁴⁵ as depicted in Fig. 14(a)-(b). Under such circumstances, the carriers excited to conduction band of the photocatalyst would be further facilitated to move towards the surfaces and thus enhance the catalytic reactions. The band bending process creates a 'lane' for the transportation of charges carriers that essentially reduces the recombination process as well⁴⁶ (Fig. 14(b)). Moreover, as these 1D structures with closely packed inter-connected nanocrystallites facilitate the carrier diffusion in the materials, it also increases the recombination resistance in these 1D nanostructures.⁴⁷ As BFO is a multiferroic material, the polarization charges on the BFO surface also favours the adsorption of dye molecules as well as enhances the charge interactions at the interfaces⁴⁸ (Fig. 14(b)). Furthermore, the reduced band gap energy also ensured that the BFO mesh would be more receptive to the visible light compared to BFO mat. Thereby, the reduced band gap energy along with the enhanced band bending processes in BFO mesh collectively accelerated the production of more number of reactive species and degraded the dye effectively.

4. Conclusion

Bismuth ferrite fibrous mat and mesh nanostructures were fabricated through the electrospinning technique wherein their

formation was essentially mediated by the collector types such as drum and plate respectively. The thermo-gravimetric weight loss curves indicated the characteristic decomposition of the as-spun samples, through which the suitable annealing temperature was estimated for the phase formation of the materials. The phase and crystal structure of the fabricated 1D nanostructures were indentified to be BiFeO₃ with rhombohedral crystal structure. XPS studies revealed that the characteristic binding energy of the respective elements confirmed the existence of elements with native oxidation states with stoichiometric ratio of BiFeO₃ phase. The FESEM and HRTEM analyses revealed the aligned structure of fibrous mat and random distribution of the mesh. The average size of the fibers in the mat and mesh was found to be 200 nm and 150 nm respectively. Optical band gap energies of mat and mesh were found to be 2.44 eV and 2.39 eV respectively. The magnetic property analysis by SQUID suggested that the origin of the magnetic properties found in these 1D nanostructures could be due to the emergence of canted spins that were manifested by the suppression of cycloidal spin structures. The magnetic properties of the nanostructures are also ascribed to the ferroelectrically induced ferromagnetism as the spin canted structures could be associated with the DM interaction that favours in the enhancement of electrical polarization property of BFO. The photocatalytic degradation of mesh was found to be greater compared to the mat, which could be essentially attributed to its intrinsic properties such as reduced band gap energy, enhanced production of [•]OH radicals, semiconductor band-bending process as well as the enhanced interaction between the BFO mesh and dye molecules. The reusability studies further confirmed the enhanced stability of both the mat and mesh nanostructures of BFO.

Acknowledgements

Authors gratefully acknowledge Prof. P. Ramamurthy, National Centre for Ultrafast Processes, University of Madras for providing the PL characterization facilities. Authors also gratefully acknowledge the Council of Scientific and Industrial Research (CSIR) for funding support (80(0074)/10/EMR-II, dt. 30-12-2010), and one of the authors M. Sakar gratefully acknowledges the NCNSNT-MHRD for the postdoctoral research fellowship (C-2/NSNT/pdf/2014/044, dt. 24-01-2014), to carry out this research work.

Notes and references

^a*National Centre for Nanoscience and Nanotechnology, University of Madras, Guindy campus, Chennai 600025, India. Fax: 044-22352494/22353309; Tel: 044-22202749, *E-mail: balasuga@yahoo.com.

- N. A. Hill, *Annu. Rev. Mater. Res.*, 2002, **32**, 1.
- J. R. Teague and R. Gerson, W. J. James, *Solid State Commun.*, 1970, **8**, 1073.
- G. Catalan and J. F. Scott, *Adv. Mater.*, 2009, **21**, 2463.
- C. A. Fernandes Vaz and U. Staub, *J. Mater. Chem. C*, 2013, **1**, 6731.
- F. Gao, Y. Yuan, K. F. Wang, X. Y. Chen, F. Chen, J. M. Liu, and Z. F. Ren, *Appl. Phys. Lett.*, 2006, **89**, 102506.
- F. Gao, X. Chen, Y. Kuibo, D. Shuai, R. Zhifeng, Y. Fang, Y. Tao, Z. Zhigang and J. M. Liu, *Adv. Mater.*, 2007, **19**, 2889.
- D. Jinyi, B. Subarna, K. M. Susanta, R. S. York and M. Mano, *Journal of Fundamentals of Renewable Energy and Applications*, 2011, Article ID R101204, 1.
- G. Renqing, F. Liang, D. Wen, Z. Fengang, and S. Mingrong, *J. Mater. Chem.*, 2011, **21**, 18645; M. I. Zaki, W. Ramadan, A. Katrib, A. I.M. Rabee, *Appl. Surf. Sci.* 2014, **317**, 929; R. He, S. Cao, P. Zhou, Jiaguo Yu, *Chinese J. Catal.*, 2014, **35**, 989.
- M. Sakar, S. Balakumar and S. Ganesamoorthy, *J. Mater. Chem. C*, 2014, **2**, 6835; G. Renqing, F. Liang, D. Wen, Z. Fengang, and S. Mingrong, *J. Phys. Chem. C*, 2010, **114**, 21390
- M. Sakar, S. Balakumar, P. Saravanan and S. N. Jaisankar, *Mater. Res. Bull.*, 2013, **48**, 2878; L. Shun, Y. H. Lin, B. P. Zhang, Y. Wang and C. W. Nan, *J. Phys. Chem. C*, 2010, **114**, 2903; W. Jie, L. Haiyang, M. Shengchun, Z. Chao, X. Zhuo and D. Brahim, *J. Mater. Sci.: Mater. Electron.*, 2012, **23**, 1869; J. Yang, L. Xu, C. Liu, T. Xie, *Appl. Surf. Sci.*, 2014, **319**, 265; C. Hao, F. Wen, J. Xiang, H. Hou, W. Lv, Y. Lv, W. Hu, Z. Liu, *Mater. Res. Bull.*, 2014, **50**, 369.
- H. Liu, Y. Li, S. Xiao, H. Li, L. Jiang, D. Zhu, B. Xiang, Y. Chen and D. Yu, *J. Phys. Chem. B*, 2004, **108**, 7744; B. Yuan, and L. Cademartiri, *L. J. Mater. Sci. Tech.*, 2014, DOI: 10.1016/j.jmst.2014.11.015.
- S. Jenny, M. Masaya, T. Masato, Z. Jinlong, H. Yu, A. Masakazu and W. B. Detlef, *Chem. Rev.*, 2014, **114**, 9919.
- B. Weng, S. Liu, Z. R. Tang, and Y. J. Xu, *RSC Adv.*, 2014, **4**, 12685.
- Z. Li, and C. Wang, *Springer Science & Business Media*, 2013, 1.
- S. Thandavamoorthy, G. S. Bhat, R. W. Tock, S. Parameswaran, S. S. Ramkumar, *J. Appl. Poly. Sci.*, 2005, **96**, 557.
- B. Vince, and W. Xuejun, *Mater. Sci. Eng. C Mater. Biol. Appl.*, 2009, **29**, 663.
- M. Sakar and S. Balakumar, *RSC Adv.*, 2013, **3**, 23737.
- A. M. B. Nasser, K. Bongsoo and Y. K. Hak, *J. Phys. Chem. C*, 2009, **113**, 531; S. Ramakrishna, K. Fujihara, W. E. Teo, T. Yong, M. Zuwei and R. Mater. *Today*, 2006, **9**, 40; W. E. Teo, R. Inai, and S. Ramakrishna, *Sci. Technol. Adv. Mater.*, 2011, **12**, 013002.
- P. M. Shaibani, K. Prashanthi, A. Sohrabi, T. Thundat, *J. Nanotechnology*, 2013, 2013, Article ID 939531, 1; L. Shao, H. Xie, J. Mo, Z. Yang, Z. Fan, C. Qi, *Environ. Eng. Sci.*, 2012, **29**, 807.
- Q. Xiang, J. Yu, P. K. Wong, *J. Colloid. Interf. Sci.*, 2011, **357**, 163; S. Kanazawa, T. Furuki, T. Nakaji, S. Akamine, R. Ichiki, *J. Phys.: Conference Series*, 2013, **418**, 012102
- I. M. Szilagyi, E. Santala, M. Heikkilä, M. Kemell, T. Nikitin, L. Khriachtchev, M. Rasanen, M. Ritala and M. Leskela, *J. Therm. Anal. Calorim.*, 2011, **105**, 73.; W. Nuansing, S. Ninmuang, W. Jarerboon, S. Maensiri and S. Seraphin, *Mater. Sci. Eng. B*, 2006, **131**, 147.
- W. Ponhan and S. Maensiri, *Solid State Sci.*, 2009, **11**, 479.
- C. Ederer and N. A. Spaldin, *Phys. Rev. B*, 2005, **71**, 060401.
- S. M. Selbach, T. Tybell, M. A. Einarsrud and T. Grande, *Chem. Mater.*, 2007, **19**, 6478.
- A. P. Grosvenor, B. A. Kobe, M. C. Biesinger and N. S. McIntyre, *Surf. Interface Anal.*, 2004, **36**, 1564; T. Toru and H. Peter, *Appl. Surf. Sci.* 2008, **254**, 2441.
- A. Tamilselvan, S. Balakumar, M. Sakar, C. Nayek, P. Murugavel, and K. Saravana Kumar, *Dalton Trans.*, 2014, 43, 5731; J. Wu, J. Wang, D. Xiao and J. Zhu, *ACS Appl. Mater. Interfaces*, 2011, **3**, 2504.

27. A. Lahmar, K. Zhao, S. Habouti, M. Dietze, C. H. Solterbeck, M. E. Souni, *Solid State Ionics*, 2011, **202**, 1.
28. X. G. Han, H. Z. He, Q. Kuang, X. Zhou, X. H. Zhang, T. Xu, Z. X. Xie and L.S. Zheng, *J. Phys. Chem. C*, 2009, **113**, 584; A. Leelavathi, M. Girdhar and N. Ravishankar, *Phys. Chem. Chem. Phys.*, 2013, **15**, 10795.
29. D. Li and Y. Xia, *Nano Lett.*, 2003, **3**, 555; D. Li and Y. Xia, *Nano Lett.* 2004, **4**, 933; S. Wolfgang, Y. Junhan, P. Hyun, M. Vasana, P. Georgios, D. Amit, T. Joshua and C. N. Juan, *J. Am. Ceram. Soc.*, 2006, **89**, 395.
30. P. D. Dimple, O. D. Jayakumar, A. K. Tyagi, K. G. Girija, C. G. S. Pillai and G. Sharma, *Nanoscale*, 2010, **2**, 1149.
31. S. V. M. Pavana, C. Karthik, R. Ubig, M. S. Ramachandra Rao and C. Sudakar, *Appl. Phys. Lett.*, 2013, **103**, 022910.
32. W. Hai, Z. Yue, M. Q. Cai, H. Haitao and L. W. C. Helen, *Solid State Comm.*, 2009, **149**, 641.
33. O. Q. JoseLuis, D. David, Z. D. Inti, A. S. Humberto, B. Israel, S. J. Patricia and N. E. Noel, *Inorg. Chem.*, 2013, **52**, 10306.
34. F. Linfeng, Y. Jikang, H. Yongming, W. Changzheng, W. Junling and W. Yu, *Cryst. Growth Des.*, 2011, **11**, 1049.
35. A. Palewicz, R. Przenioslo, I. Sosnowska and H. W. Hewat, *Acta Crystallogr.* 2007, **63**, 537; J. Clark and Robertson, *J. Appl. Phys. Lett.* 2007, **90**, 132903.
36. F. Huang, Z. Wang, X. Lu, J. Zhang, K. Min, W. Lin, R. Ti, T. Xu, J. He, C. Yue and J. Zhu, *Sci. Rep.*, 2013, **3**, 2907.
37. H. Feng, *J. Magn. Magn. Mater.*, 2010, **322**, 1765.
38. C. Ederer and C. J. Fennie, *J. Phys.: Condens. Matter*, 2008, **20**, 434219.
39. D. L. Fox and J. F. Scott, *J. Phys. C: Solid State Phys.*, 1977, **10**, L329.
40. S. R. Morrison, *Electrochemistry at Semiconductor and Oxidized Metal Electrode*, PlenumPress, NewYork, 1980, 416.
41. H. Hotop, W. C. Lineberger, *J. Phys. Chem. Ref. Data*, 1975, **4**, 539; T. Andersen, H. K. Haugen, H. Hotop, *J. Phys. Chem. Ref. Data*, 1999, **28**, 1511.
42. B. H. J. Bielski, D. E. Cabelli, *Active Oxygen in Chemistry*, C. S. Foote, J. S. Valentine, A. Greenberg, J. F. Liebman, *Superoxide and Hydroxyl Radical Chemistry in Aqueous Solution*, Springer, Netherlands, 1995, 66-104; J. F. Dai, T. Xian, L. J. Di, H. Yang, *J. Nanomaterials*, **2013**, 2013, Article ID 642897, 5
43. A. L. Linsebigler, G. Lu, and J. T. Jr. Yates, *Chem. Rev.*, 1995, **95**, 735.
44. S. Park, C. W. Lee, M. G. Kang, S. Kim, H. J. Kim, J. E. Kwon, S. W. Park, C. Y. Kang, K. S. Hong and K. T. Nam, *Phys. Chem. Chem. Phys.* 2014, **16**, 10408.
45. Z. Zhang and J. T. Jr. Yates, *Chem. Rev.*, 2012, **112**, 5520; L. Li, P. A. Salvador and G. S. Rohrer, *Nanoscale*, 2014, **6**, 24.
46. M. Sakar, S. Balakumar, I. Bhaumik, P. K. Gupta and Jaisankar, *RSC Adv.*, 2014, **4**, 16871; Y. Cui, J. Briscoe and S. Dunn, *Chem. Mater.*, 2013, **25**, 4215.
47. E. Naveen Kumar, J. Rajan, P. S. Archana, C. Vijila and S. Ramakrishna, *J. Phys. Chem. C*, 2012, **116**, 22112; M. Kunal, T. H. Teng, J. Rajan and S. Ramakrishna, *Appl. Phys. Lett.*, 2009, **95**, 012101.
48. S. Matt and S. Dunn, *J. Phys. Chem. C*, 2012, **116**, 20854; B. Matthias, *Energy Environ. Sci.*, 2011, **4**, 3275.